Characterisation of the Optical Turbulence at Siding Spring

Michael Goodwin[1,3,4], Charles Jenkins[1,5] and Andrew Lambert[2]

[1]Research School of Astronomy Astrophysics, Australian National University, Mt Stromlo Observatory, via Cotter Rd, Weston, ACT 2611, Australia
[2]School of Engineering and Information Technology, UNSW@ADFA, Canberra, ACT 2600, Australia
[3]Corresponding author. Email: mgoodwin@aao.gov.au
[4]Current address: Australian Astronomical Observatory, PO Box 915, North Ryde, NSW 1670, Australia
[5]Current address: Earth Science and Resource Engineering, CSIRO

Abstract

Measurements of the optical turbulence profile above Siding Spring Observatory were conducted during 2005 and 2006. This effort was largely motivated by the need to predict the statistical performance of adaptive optics at Siding Spring. The data were collected using a purpose-built instrument based on the slope detection and ranging (SLODAR) method where observations of a bright double star are imaged by Shack–Hartmann taken with the Australian National University 24-inch and 40-inch telescopes. The analysis of the data yielded a model consisting of a handful of statistically prominent thin layers that are statistically separated into the ground layer (37.5, 250 m) and the free atmosphere (1, 3, 6, 9, 13.5 km) for good (25%), typical (50%), and bad (25%) observing conditions. We found that ground-layer turbulence dominates the turbulence profile with up to 80% of the integrated turbulence below 500 m. The turbulence tends to be non-Kolmogorov, especially for the ground layer with a power-law index of $\beta \sim 10/3$. The mirror/dome seeing can be a significant fraction of the ground-layer turbulence. The median atmospheric seeing is around 1.2 arcsec, in agreement with observational reports.

Keywords: atmospheric effects, instrumentation: adaptive optics, instrumentation: miscellaneous, site testing

1 INTRODUCTION

Of interest is the performance of adaptive optics (AO) at Siding Spring Observatory (SSO), Australia. The motivation for turbulence profiling at SSO is to understand the structure of atmospheric turbulence at a moderate quality astronomical site and to determine the performance predictions for AO. It is known that the performance of AO strongly depends on the structure of the atmospheric turbulence (Hardy 1998). No previous detailed site testing of the structure of atmospheric turbulence (strength and speed) has been undertaken at SSO. The improvements in cost, availability, and technology make AO a worthy study at such moderate seeing sites such as SSO. AO significantly improves the image quality by compensating for the aberrations induced by atmospheric turbulence in real time. The performance of an AO system can be predicted with simulation codes using input atmospheric model optical turbulence profiles (model-OTP) that characterise the turbulence above the astronomical site. It could be that the installation of AO for the 3.9-m Anglo-Australian Telescope (AAT) may open the door for new science programmes and discoveries that would lead to better science.

If the bulk of the turbulence is low at SSO, then the ground-layer adaptive optics (GLAO) correction mode can provide significant gains. GLAO provides a large field of view (FoV; 6 arcmin), but with a partial AO correction (Hubin et al. 2006). Certain science cases (including cosmology and extragalactic observations) require larger FoVs with excellent seeing conditions, which can be achieved with GLAO for a larger fraction of nights (Hubin et al. 2006). The GLAO correction mode averages the wavefront from several or more widely separated wavefront sources and applies the result to a single deformable mirror conjugated at the ground. Hence, GLAO performance is typically best when the bulk of turbulence is near the ground. It is known that the bulk fraction of atmospheric turbulence at most astronomical sites is located near the ground (Hardy 1998), in the 'boundary layer' below 500 m in altitude. The figure of merit for the GLAO correction mode is the ensquared energy (EE) fraction in a pixel. In some cases, the improvement in ensquared energy can be more than double the natural seeing and hence halves the integration times to achieve the same signal-to-noise ratios (S/N; Hubin et al. 2006).

Hence, the observations of turbulence profiles are of critical importance as the statistical analysis reveals a set of model optical turbulence profiles that serve as input atmospheres into AO simulation codes. This fact has provided

1

the necessary justification for turbulence ranging campaigns at major astronomical sites as well as research into various site-testing instruments.

The characteristic structure of the atmospheric turbulence above SSO was not well understood prior to our site-testing campaign. However, the seeing resulting from the total turbulence integral is better understood with differential image motion monitor (DIMM) seeing measurements at SSO reported by Wood, Rodgers, & Russell (1995). The common seeing values reported by Wood et al. (1995) are 1.2 arcsec. Several turbulence profiles have been observed above SSO (1997 January) using the generalised scintillation detection and ranging (SCIDAR) method with the Australian National University (ANU) 40-inch telescope and are reported by Klueckers et al. (1998) where it is noted that the strongest turbulent layers are located near the ground in the so-called boundary layer with heights below 3 km. However, a statistically robust model-OTP cannot be derived due to an insufficient number of profiles observed by Klueckers et al. (1998).

This paper discusses the $C^2_N(h)$ and $V(h)$ profile measurements taken at SSO and the derived model-OTP for suitable use in AO simulation codes. Section 2 introduces the turbulence parameters. Section 3 outlines the technique and instrumentation used in the measurement of the $C^2_N(h)$ and $V(h)$ profiles. Sections 4 and 5 discuss the data and trends noted in the measured profiles. Section 6 introduces the model-OTP that characterises the atmospheric turbulence profile at SSO. Concluding remarks are in Section 7.

The predicted performance of AO at SSO based on the presented model-OTP will be published in a forthcoming paper.

2 TURBULENCE PARAMETERS

Atmospheric turbulence exhibits a physical process that is complex and random in nature, requiring a suitable model. A widely accepted model is that proposed by Kolmogorov (Hardy 1998), who investigated the mechanical structure of atmospheric turbulence. The Kolmogorov model described the velocity of motion in a fluid medium, where energy is added in the form of large-scale disturbances, which then break down to smaller and smaller structures, until an inner scale is reached.

From the Kolmogorov model, a spatial power spectrum of phase (power-law index, $\beta = 11/3$) can be deduced followed by a set of structure functions that describe non-stationary random fluctuations encountered by atmospheric turbulence. Using these structure functions, a set of general turbulence parameters can be specified that summarise the effects of atmospheric turbulence. The key parameter used in the calculation of the turbulence parameters is the refractive index structure constant, C^2_N (units $m^{-2/3}$), and its variation with altitude, z, and time, t. We now proceed with the specification of the most useful turbulence parameters for AO.

The full width at half-maximum (FWHM) seeing angle or image dispersion for long exposure images, ϕ (rad), is given by

$$\phi = \frac{\lambda}{r_0}, \tag{1}$$

$$r_0 = 0.185\lambda^{6/5}(\sec\zeta)^{-3/5}\left[\int_z C_n^2(z)\mathrm{d}z\right]^{-\frac{3}{5}}, \tag{2}$$

where λ (m) is the wavelength and r_0 (m) is the coherence length (Fried 1966). Partial AO compensation results in a diffraction-limited core surrounded by a broader halo equal to the seeing disc, ϕ. The parameter r_0 includes the integrated effect of the refractive index fluctuations over the vertical propagation path, z (m). It represents a fictitious 'cell size' of turbulence and defines an aperture diameter over which the mean-square wavefront error is 1 rad^2 given by where ζ (rad) is the zenith angle. The coherence length, r_0, also corresponds to the approximate spatial scale that AO must measure and compensate the effects of atmospheric turbulence. The angular displacement over which the mean-square wavefront error is 1 rad^2 is called the isoplanatic angle (Fried 1982), θ_0 (rad), given by

$$\theta_0 = 0.058\lambda^{6/5}(\sec\zeta)^{-8/5}\left[\int_z C_n^2(z)z^{5/3}(z)\mathrm{d}z\right]^{-\frac{3}{5}}. \tag{3}$$

The isoplanatic angle, θ_0, can be considered the approximate compensated FoV for on-axis single-conjugate AO or the maximum allowable angular distance from the high-order wavefront source to the science object. The coherence time (Greenwood 1977), τ_0 (s), is roughly the time taken for the wind to move turbulence by r_0. This is given by

$$\tau_0 = 0.058\lambda^{6/5}(\sec\zeta)^{-3/5}\left[\int_z C_n^2(z)v_{\mathrm{wind}}^{5/3}(z)\mathrm{d}z\right]^{-\frac{3}{5}}. \tag{4}$$

The coherence time, τ_0, can be considered as the maximum duration that the atmospheric turbulence can be considered 'frozen', or the maximum duration allowable between sequential wavefront samples and corrections for the AO control system.

Common site-testing instruments that measure atmospheric turbulence usually assume a Kolmogorov model of turbulence with power-law index, $\beta = 11/3$. All of these parameters can also be measured in the case of non-Kolmogorov turbulence but they all become functions of β. To estimate the performance of optical systems in non-Kolmogorov turbulence, the power spectral density can be expressed (Stribling, Welsh, & Roggemann 1995) as

$$\Phi_n(\kappa, \beta, z) = a(\beta)B(z)\kappa^{-\beta}, \tag{5}$$

where $\Phi_n(\kappa, \beta, z)$ is the power spectral density as a function of position, z is along the optical path, β is the power-law

slope (11/3 for Kolmogorov), $B(z)$ is the index structure constant having units $m^{3-\beta}$, and $a(\beta)$ is a function to maintain consistency with the index structure function and is given by Stribling et al. (1995) as

$$D_n(r) = B(z)r^{\beta-3}. \qquad (6)$$

The analysis of the non-Kolmogorov model is appropriate given that the value of the power-law index, β, can be determined by the function-fitting SLODAR (slope detection and ranging) method (Butterley, Wilson, & Sarazin 2006).

3 TURBULENCE MEASUREMENT

Various methods are used for turbulence profiling, including direct sensing with microthermal sensors on towers (Pant, Stalin, & Sagar 1999) or balloons (Azouit & Vernin 2005), remote sensing with acoustic scattering (sonic detection and ranging (SODAR); Travouillon 2006), or triangulation of scintillation (SCIDAR; Vernin & Roddier 1973; Fuchs, Tallon, & Vernin 1994) or of image motion (SLODAR; Wilson 2002; Butterley et al. 2006; Goodwin, Jenkins, & Lambert 2007). These techniques have reached a degree of maturity, exhibiting reasonable agreement when used together in campaigns (Tokovinin & Travouillon 2006; Cerro Tololo campaign, Sarazin et al. 2005). Each technique has its unique benefits and limitations in terms of cost, height resolution, height range, temporal resolution, ease of implementation, and data reduction complexity.

3.1 SLODAR Method

The SLODAR technique has been used on large telescopes at the ORM, La Palma, and later on a portable, stand-alone, turbulence profiler for European Southern Observatory (ESO), based on a 40-cm telescope with an 8×8 Shack–Hartmann wavefront sensor (SHWFS; 5-cm-sized sub-apertures; Wilson 2002). The larger apertures 5–15 cm of SLODAR relax exposure times to 4–8 ms (typical wind-crossing timescales), providing more suitable observational targets. The ground layer can be measured with sufficient height resolutions (50–100 m) by observing widely separated double stars (Wilson 2002), whereas higher altitudes can be investigated by observing more narrowly separated doubles. For these reasons, we have selected the SLODAR method for our site-testing campaign to measure and characterise the turbulence profiles at SSO.

The SLODAR method, illustrated in Figure 1, is an optical triangulation method with the turbulence information extracted from the cross-covariance of the wavefront slopes of a double star measured using an SHWFS. The two optical wavefront components of the double star with separation θ, passing through a single turbulent layer, at altitude H, produce copies of the aberrations at the telescope pupil that are displaced by $S = H\theta$ along the axis of the double star separation. The corresponding turbulent layer shows up in the
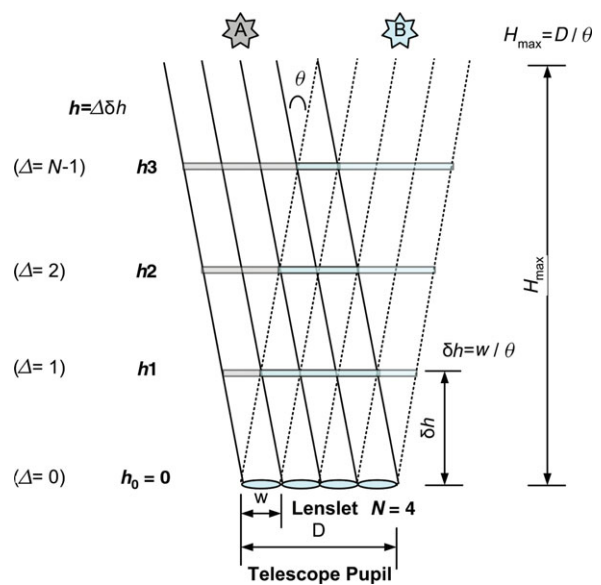
Figure 1. Diagram illustrating the geometry of the SLODAR method for a $N = 4$ system. θ is the double star angular separation. D is the diameter of the telescope pupil and w is the width of the sub-aperture of the SHWFS array. The centres of the altitude bins are given by $\Delta\delta h$, where Δ is the lateral pupil separation (units of w) and $\delta h = w/\theta$. The ground layer can be analysed in higher resolution by utilisation of double stars having larger θ.

spatial cross-covariance of the optical wavefronts at a spatial offset S.

The SHWFS measures the wavefront slopes by optically dividing the telescope pupil into an $(N \times N)$ array of square sub-apertures, accompanying each lens in a microlens array and measuring the centroids of the spot displacements, being proportional to the averaged wavefront slope. The sub-apertures and the detector have a sufficient FoV to measure the $(N \times N)$ array of spot patterns from both components of the double star simultaneously. The exposure times are typically 4–8 ms to freeze the turbulence, being directly proportional to the sub-aperture size, w, related to the wind speed, v, with crossing timescales, $\tau = w/v$. The sub-aperture sizes are designed to be approximately equal to or less than r_0, or ranging from 5 cm (poor seeing) to 15 cm (good seeing), depending on the median seeing.

The height resolution is uniform, given by $\delta h = w/\theta$ (at zenith). The highest sampled layer, $h_{N-1} = (N-1)\delta h \approx H_{max} = D/\theta$, where N is the number of sub-apertures across the telescope pupil, with the ground layer denoted as $h_0 = 0$ with resolution $\delta h/2$. The vertical resolution and maximum sample height are scaled by the inverse of the air mass, χ, or $\cos(\zeta)$, where ζ is the zenith distance.

3.2 SLODAR Instrument

The SLODAR site-testing campaign to characterise the atmospheric turbulence above SSO consists of results that were obtained from eight 1-week observing runs spanning years 2005 to 2006 with the purpose-built 7×7 (runs 1–6) and
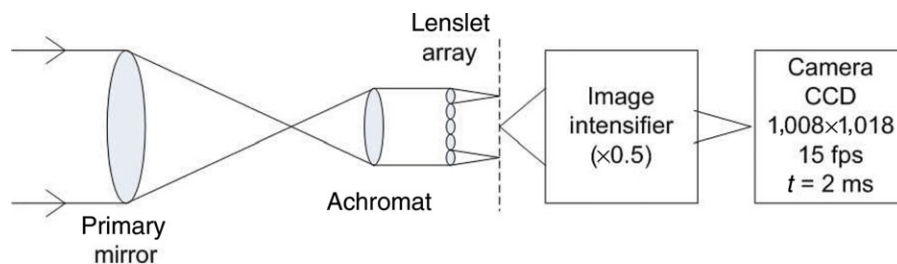
Figure 2. The expanded optical block diagram of the 7 × 7 SLODAR instrument (first version) that attaches via bayonet mounted to the focus of the ANU 24-inch telescope at SSO. The diagram shows 5 × 5 SHWFS for simplification.
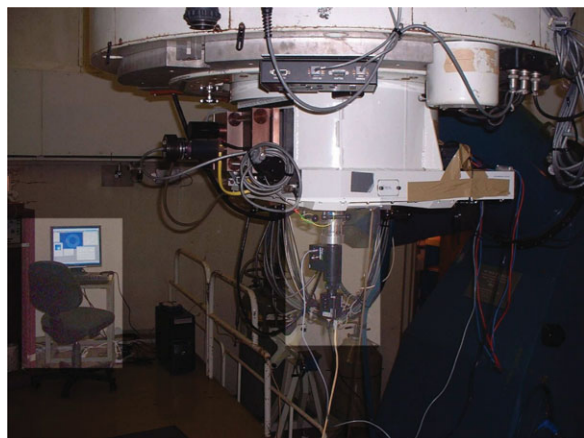

Figure 3. The ANU 17 × 17 SLODAR instrument (5.8-cm sub-apertures) on the ANU 40-inch telescope at SSO (photograph taken on 2006 June 18).

17 × 17 (runs 7 and 8) SLODAR instrument configurations using the ANU 24-inch and 40-inch telescopes.

The SLODAR instrument can be compared with that of an SHWFS as used in AO to measure the aberrated optical wavefront. However, the SHWFS of the SLODAR instrument has a much wider FoV requiring the simultaneous measurement of double star optical wavefront gradients. The double stars observed by SLODAR can have angular separations up to several arcminutes. A functional diagram of the first ANU 7 × 7 SLODAR instrument installed on the ANU 24-inch telescope at SSO is shown in Figure 2. The optical diagram for the 17 × 17 SLODAR instrument on the ANU 40-inch telescope is similar to that shown in Figure 2 except for the 2 × 2 optic before the image intensifier. The 17 × 17 SLODAR instrument is shown in Figure 3.

An advantage of the SLODAR instrument is a relatively simple optical design. A single collimator lens images the telescope pupil onto the microlens array (MLA) as shown in Figure 2. The collimating lens performs the following functions: (i) de-magnifies and collimates the incoming light beams of each double star component (i.e. point source at infinity); (ii) re-images the telescope pupil onto the MLA.

The MLA performs the function of optically dividing the telescope pupil into an array of sub-apertures. Each sub-aperture forms two spots (image of the double star) at their focal plane with image motion caused by aberrations in the double star optical wavefronts. The width of the sub-apertures, w, is comparable to the seeing coherent length, r_0, keeping the aberrated optical wavefront approximately linear. The sub-aperture spot displacement from mean position (centroid) is proportional to the averaged wavefront gradient (or slope). The images of the telescope pupils formed at the MLA are completely overlapped and are produced by double star components A and B. The individual lenslets (or sub-apertures) typically have slow focal ratios that image double star A and B components onto the image intensifier input (photocathode).

The image intensifier performs the function of applying a high gain ($>1\,000$) to the incoming signal photons overcoming the high read noise of the high frame rate cameras used with the SLODAR instruments. The image intensifier allows fainter double stars to be observed, down to limiting magnitudes in the V band of approximately 5–6 (compared with 1–2 without the image intensifier). The image intensifier re-images and de-magnifies the MLA spot patterns onto the camera detector. Hence, the SLODAR instrument has two focal planes requiring correct adjustments during the calibration process.

The camera detectors used with the SLODAR instruments have the key features: (i) large format cameras (e.g. 1018 × 1008 pixel array) to image wide double stars; (ii) high frame rates (15, 20, 30, 200 fps) for layer wind speed measurements; (iii) short camera exposures of 2–8 ms in order to 'freeze' the turbulence. The camera exposures are on timescales equivalent to the turbulent-layer wind-crossing times of the sub-apertures.

Complementing the 17 × 17 instrument was the purpose-built real-time software (a graphical user interface (GUI) application), to satisfy the requirements for instrument control, processing and diagnostics, and autonomously logging of centroid data. The real-time software significantly increased the number of quality observed data sets.

4 DATA DESCRIPTION

4.1 Observational Plan

The scheduled observing runs for the SSO turbulence profiling are listed in Table 1. The observational plan was to sample

Table 1. SLODAR Observational Runs at SSO

Run	Scheduled Dates	Nights	Profiles	Telescope (inch)/Instrument
1	2–8 May 2005	4 of 7	–	ANU 24/7 × 7 SLODAR
2	14–20 June 2005	3 of 7	31	ANU 24/7 × 7 SLODAR
3	21–27 September 2005	3 of 7	86	ANU 24/7 × 7 SLODAR
4	1–7 November 2005	1 of 7	16	ANU 24/7 × 7 SLODAR
5	12–18 December 2005	2 of 7	37	ANU 24/7 × 7 SLODAR
6	18–24 January 2006	5 of 7	136	ANU 24/7 × 7 SLODAR
7	11–17 April 2006	5 of 7	450	ANU 40/17 × 17 SLODAR
8	15–21 June 2006	6 of 7	1892	ANU 40/17 × 17 SLODAR

Table 2. Double Star Targets for SLODAR Observations at SSO

Name	α (RA)	δ (Dec.)	Mag	Separation (arcsec)
θ Eri	02 58	−40 18	3.4/4.5	8.2
DUN 16 Eri	03 49	−37 37	4.8/5.3	7.9
θ Ori	05 35	−05 25	4.9/5	135
β Mon	06 28	−07 02	4.7/5.2	7.2
α Cru	12 26	−63 06	1.3/1.8	4.3
μ Cru	12 55	−57 11	4.0/3.5	34.9
HIP65271	13 23	−60 59	4.5/6.1	60
α Cen	14 39	−60 50	− 0.01/1.33	9.5
θ Ser	18 56	+04 12	4.6/4.9	21.6
δ Aps	16 20	−78 42	4.7/5.3	102.9

the turbulence profile for each season over the course of the whole year. Turbulence profiling results were obtained from eight 1-week observational runs spanning years 2005 to 2006 with the 7×7 (runs 1–6) and 17×17 (runs 7 and 8) SLODAR instruments using the ANU 24-inch and 40-inch telescopes, respectively. Sampling over three consecutive months was conducted from 2005 November to 2006 January to examine any possible monthly variation in turbulence profiles. The first observational run in 2005 May provided a test run of the 7×7 SLODAR instrument on the ANU 24-inch telescope. A total of six observing runs were conducted with the ANU 7×7 SLODAR instrument, the final run being in 2006 January. The instrument changeover for the observational run in 2006 April to the 17×17 SLODAR instrument on the ANU 40-inch telescope was a response to the scientific requirement of needing more height sampling resolution bins and the measurement of the turbulent-layer wind speeds.

The observational list of double star targets is tabulated in Table 2. The limiting magnitude of the instruments, $V \sim 5.5$, limited the observational list to a couple (on occasions only one) of suitable targets for any given time at the telescope. The ability to alternate between ground-layer and free-atmosphere sampling is facilitated by switching between widely to narrowly separated double star targets. The increased number of profiles (data sets) for the final two observing runs was a result of changing from the manual process of logging data to automated logging with the introduction of the real-time software. The final run in 2006 June witnessed the full operation of the real-time software which captured 1 892 data sets for off-line processing.
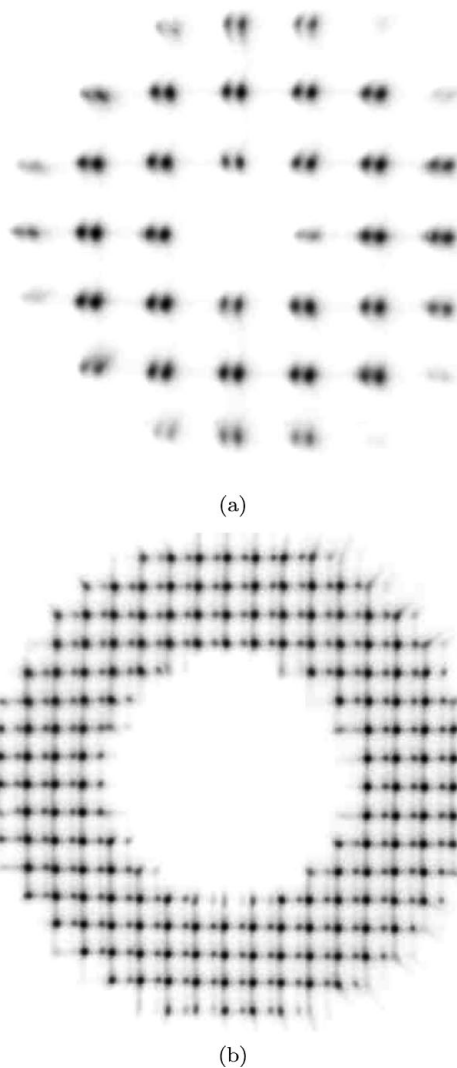
(a)

(b)

Figure 4. An ensemble average over raw camera frames of (a) the SLODAR 7×7 instrument on the ANU 24-inch telescope at SSO and (b) the SLODAR 17×17 instrument on the ANU 40-inch telescope at SSO. The double stars observed are (a) $\alpha Crux$ and (b) αCen are aligned along the SHWFS x-direction.

4.2 Data Acquisition

The SLODAR instrument delivers raw camera frames as shown in Figure 4 and are processed either by MATLAB (MathWorks 2005) (ANU 7×7 SLODAR instrument) or by the SLODAR real-time software (ANU 17×17 SLODAR instrument). The SLODAR real-time software has the capability to log raw camera frames but typically only the centroid data are logged.

A summary of the observational data statistics is listed in Table 1. Data are acquired at 15 fps (Pulnix; JAI Inc. 2009, TM1020, 1 018 × 1 008 pixels) and 30 fps (Pixelink; PixeLINK 2009, A741, 1 280 × 1 024 pixels) to image larger separated double stars and 200 fps (Pulnix TM6740GE, 640 × 480 pixels) for high temporal sampling. A typical data set
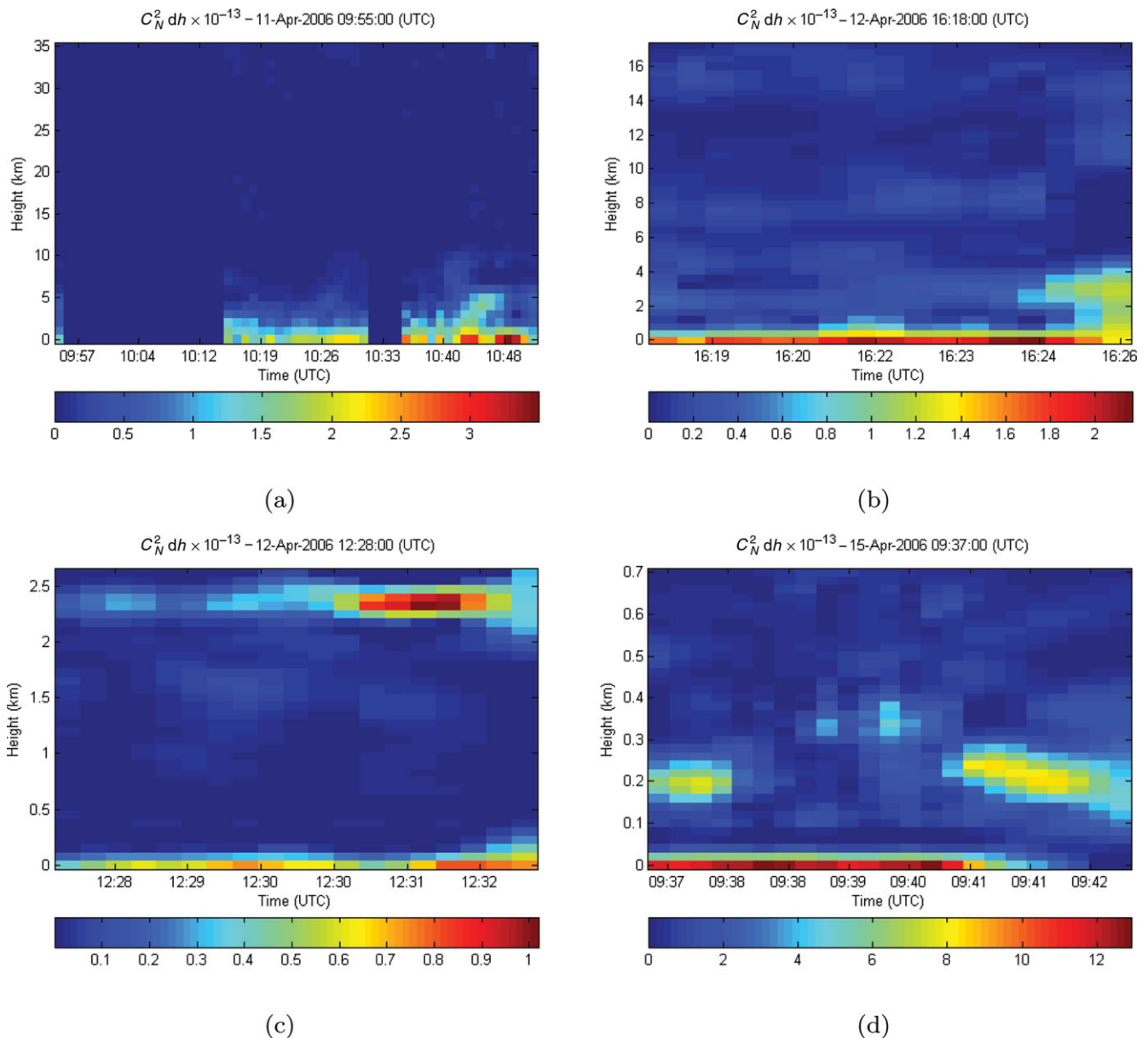
Figure 5. SSO run 7. Examples of consecutive SLODAR turbulence profiles from difference spaced double star targets (height ranges). Each temporal plot represents a group of data sets from the same double star target (similar height sampling) measured during 2006 April 11–17. The vertical axis denotes height (km) and the horizontal axis denotes time (UTC). The colour denotes turbulence strength, $C_N^2(h)\mathrm{d}h$ ($m^{4-\beta}$). The plots are derived by interpolating the turbulence profiles onto a regular spaced grid at approximately Nyquist sampling. The blank regions represent times having no data. Note, $h = 0$ km defines the height of the telescope's primary mirror.

consists of a minimum of 600 camera frames (15 fps) or 4 000 camera frames (200 fps) for sufficient statistical sampling of the atmospheric turbulence.

5 DATA ANALYSIS

5.1 $C_N^2(h)$ Profiles

In this section, we provide examples of consecutive $C_N^2(h)$ turbulence profiles taken from the same double star target (or 'group' data sets having similar time stamps and height

sampling) during the seventh observing run (2006 April 11–17) and the eighth observing run (2006 June 15–21). Note that we use the convention that $h = 0$ km defines the height of the telescope's primary mirror. These observing runs had the highest number of data sets logged (see Table 1) and provide a useful visual indicator of the spatial–temporal evolution of the turbulence. Consecutive profiles for the seventh run are plotted in Figure 5. Example individual turbulence profiles from these group data sets are plotted in Figure 6.

The temporal plots of the turbulence profiles show a number of dynamical characteristics: (i) intense turbulence
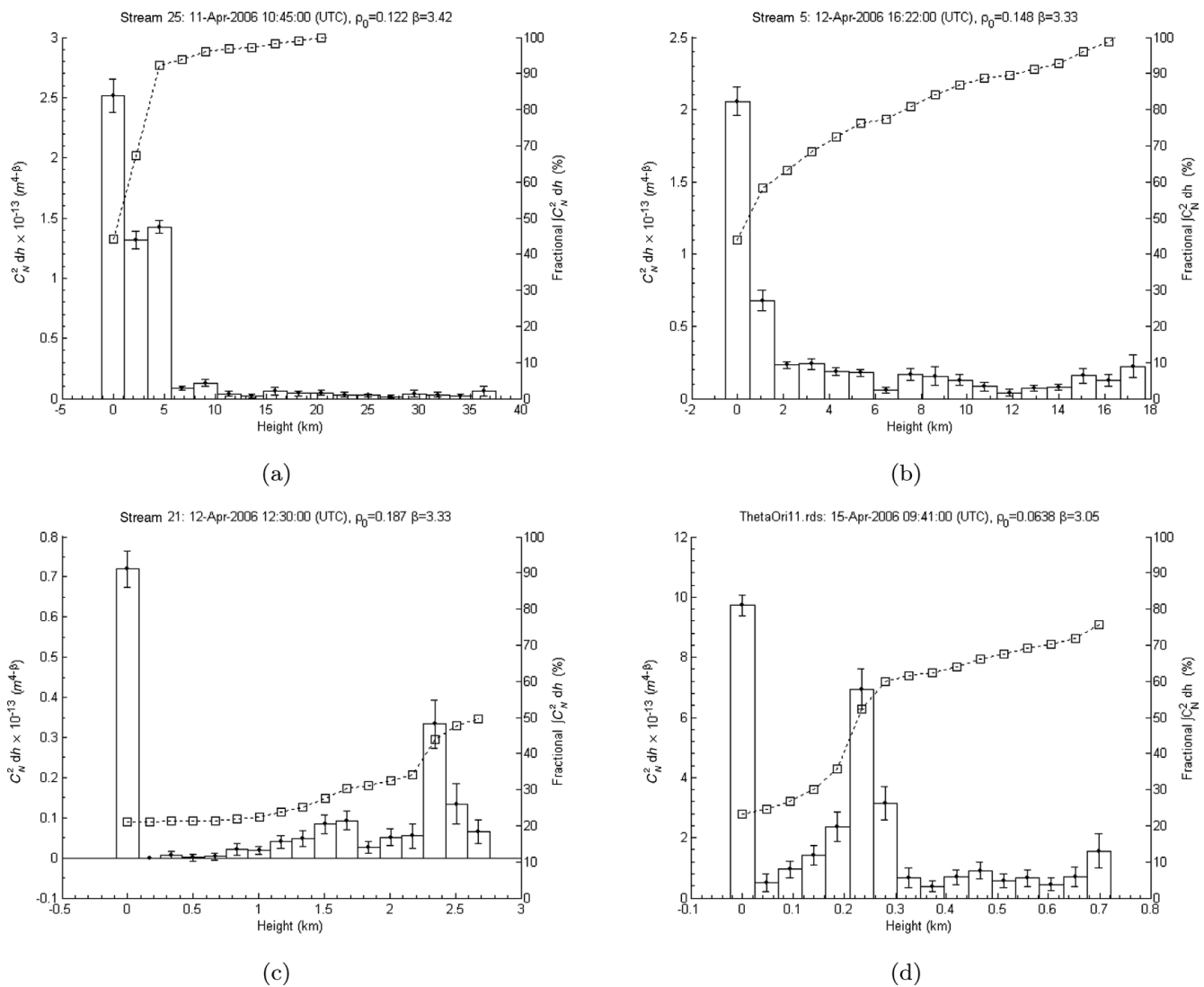
Figure 6. SSO run 7. Examples of individual SLODAR turbulence profiles with each plot representing a single profile as represented in temporal plots of Figure 5 measured during 2006 April 11–17. The vertical axis denotes turbulence strength, $C_N^2(h)\mathrm{d}h$ $(m^{4-\beta})$, and the horizontal axis denotes height (km). Note, $h = 0$ km defines the height of the telescope's primary mirror.

occurring near the ground (below 100 m); (ii) turbulent layers that can fluctuate in intensity, appearing in 'bursts' with timescales of several minutes; this can have implications for different lines of sight; (iii) appearance to drift in altitude on some occasions rather than disperse before disappearing.

To quantify the structural distribution of the atmospheric turbulence, two statistical parameters are defined, namely h_{nnnn}. The h_{nnnn} parameter describes the fractional amount (0.0 to 1.0, with 1.0 being 100%) of turbulence below *nnnn* m as measured from the telescope's primary mirror. The default value for *nnnn* is 500 m or h_{500}, but due to coarse height resolution sampling, the value of *nnnn* can be larger, e.g. 750 m or h_{750}. The h_{nnnn} allows a qualitative assessment for the performance of ground-layer AO, which is favourable if the bulk of the turbulence is near the ground.

The third statistical parameter characterises the power-law slope index of the power spectrum of spatial phase fluctua-

tions, β_{avg}. The parameter β_{avg} is representative of the entire atmospheric turbulence or averaged contribution of all layer heights. The β_{avg} was determined by the best fit of the $\Delta = 0$ theoretical covariance impulse response function for β ranging from 19/6 to 23/6 to the observed auto-covariance function, see Butterley et al. (2006). The implications of non-Kolmogorov turbulence ($\beta \neq 11/3$) in the measurement of atmospheric turbulence and astronomical imaging are discussed by Stribling et al. (1995) and Goodwin (2009).

Fits of a non-Kolmogorov exponent to the SLODAR power spectrum (auto-covariance) are not provided in this paper. The fitted data have comparable error bars to Butterley et al. (2006) and that the best fit within the error bars typically produces exponent values that are non-Kolmogorov (less than 11/3). An exponent less than 11/3 causes the DIMM seeing to be overestimated due to increased image motion for small apertures (Goodwin 2009). The power spectrum is relatively

insensitive to the outer scale (Von Karman power spectrum) as noted by Butterley et al. (2006). A fit of the outer scale would typically need an outer scale smaller than the telescope (1 m), which is not typical of other measurements at other observatories (20–40 m). The outer-scale fit also has typically larger residuals for the larger offsets in the covariance function compared with the exponent fit.
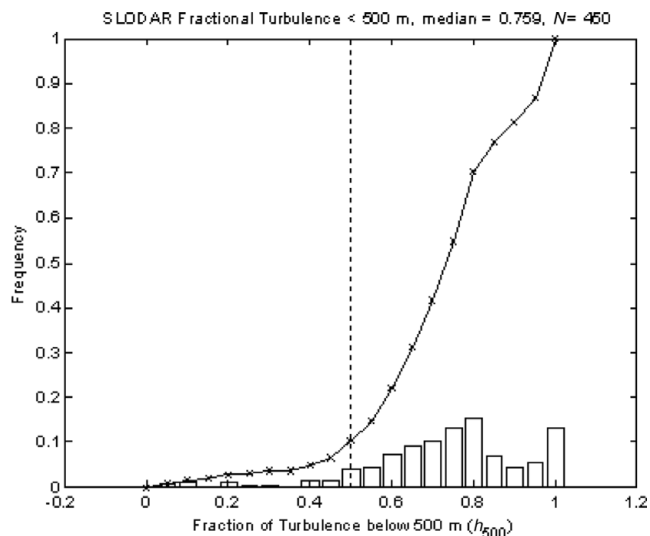
The results measured during 2006 April 11–17 (run 7) and 2006 June 15–21 (run 8) using the ANU 17 × 17 SLODAR instrument on the ANU 40-inch telescope indicate an atmospheric turbulence structure that is dominated by strong ground-layer turbulence. This is evident in the summary h_{500} parameter for all nights as shown in Figure 7. The summary h_{500} parameter indicates that nearly 76% (run 7) and 91% (run 8) of the integrated turbulence is below 500 m. Note that in a few cases of limited height resolution sampling, h_{500} will be more representative of higher altitudes, e.g. h_{750}, but this is a minority of the data sets.

The summary β_{avg} parameter for all nights is shown in Figure 8. The summary β_{avg} parameter is found to have a median of 3.32 (run 7) and 3.35 (run 8) as compared with a Kolmogorov value of 3.67. This implies that the strong ground layer is non-Kolmogorov, causing a low β_{avg}.

The summary seeing (for a wavelength of 0.5 μm) derived from the SLODAR function-fitting method (non-Kolmogorov analysis) and the DIMM method (Kolmogorov) is shown as a histogram in Figure 9. The median seeing values for the non-Kolmogorov and DIMM analysis (using SLODAR data) are 0.77 and 1.13 arcsec (run 7) and 1.1 and 1.33 arcsec (run 8). The discrepancy between the SLODAR (non-Kolmogorov) and DIMM (Kolmogorov) seeing calculation methods is most likely due to the low β_{avg} values in the data (strong non-Kolmogorov effects). It is important to note that the seeing values have the mirror/dome seeing component removed (Goodwin et al. 2007), which is usually found to be a significant component. We note that the DIMM seeing of the SLODAR data, 1.13 and 1.33 arcsec, brackets the historical DIMM seeing measurements by Wood et al. (1995) of 1.25 arcsec.

5.2 $V(h)$ Profiles

The translational velocity information of the turbulent layers can be retrieved by introducing gradual temporal offsets, δt, in the spatial cross-covariance function of wavefront gradients and by observing the corresponding displacement of peaks (Wilson 2002). The temporal offsets, δt, are integer multiples of the camera acquisition time (inverse of frame rate) and, therefore, must be sufficiently short to capture multiple observations of the turbulent layer as it moves across the telescope pupil. Typically, $\delta t < 100$ ms, with camera acquisition times between 5 and 50 ms. A turbulent layer moving at velocity, v, will have its cross-covariance peak shifted by $v\delta t$ from its location at $\delta t = 0$, aligned along the separation axis of the double star. By making several measurements of the spatial shifts in the cross-covariance peak for several sequen-
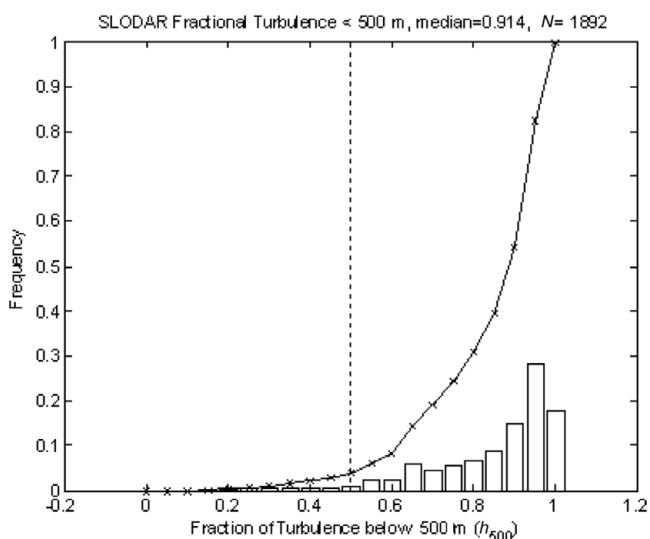
Figure 7. Summary plot showing the fraction of turbulence below 500 m based on all observable nights measured during (a) SSO run 7: 2006 April 11–17 with the median fractional amount of turbulence below 500 m at 76% (based on 450 data sets); (b) SSO run 8: 2006 June 15–21 with the median fractional amount of turbulence below 500 m at 91% (based on 1 892 data sets).

tial temporal offsets, δt, it is possible to trace the turbulent layer back to the origin to determine both height and velocity information. Examples of a layer wind speed measurement using the temporal spatial cross-covariance of centroid data during the seventh observing run (2006 April 11–17) are shown in Figure 10.

6 MODEL-OTP

A model-OTP is required to summarise the main characteristics of the measured atmospheric turbulence so that AO
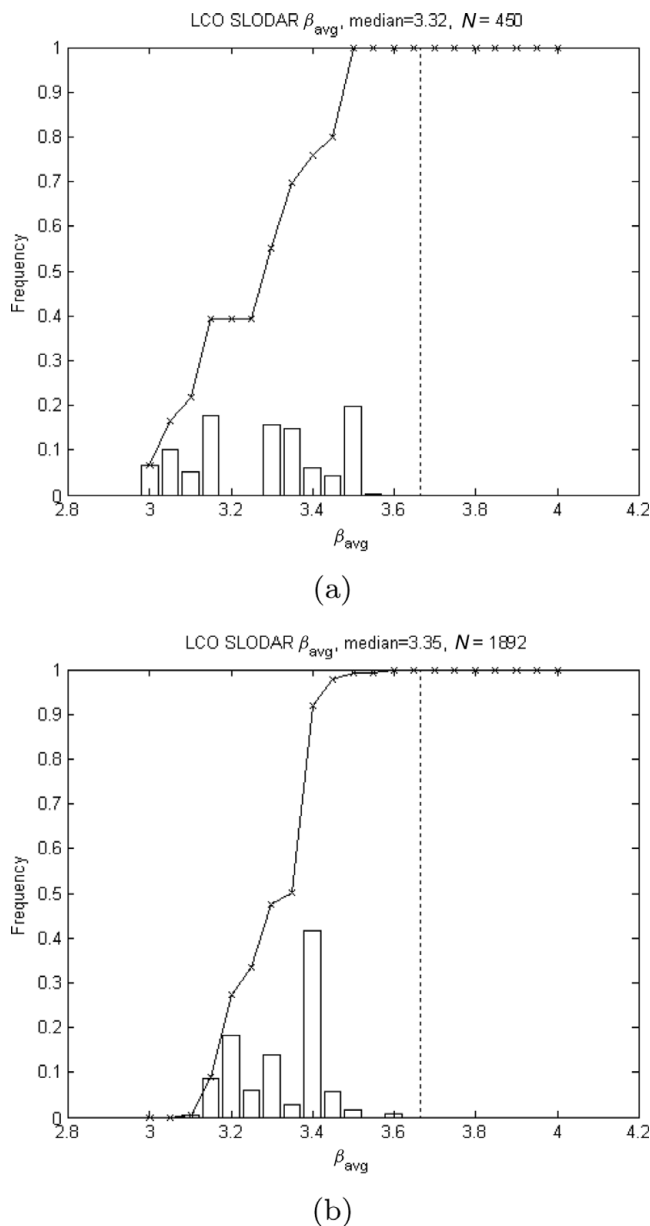
(a)

(b)

Figure 8. Summary plot showing the average power-law slope, β_{avg}, of the spatial power spectrum of phase fluctuations based on all observable nights measured during (a) SSO run 7: 2006 April 11–17 with the median of 3.32 (based on 450 data sets) and (b) 2006 June 15–21 with the median of 3.35 (based on 1 892 data sets). For both cases, the values are noticeably less than the Kolmogorov value of 3.67 (dashed vertical line).

(a)

(b)

Figure 9. Summary plot showing the seeing histograms of the SLODAR (non-Kolmogorov, red) method and DIMM (Kolmogorov, blue) method based on all observable nights measured during (a) SSO run 7: 2006 April 11–17 (based on 450 data sets) and (b) 2006 June 15–21 (based on 1 892 data sets). For both cases, the seeing values are reported at a wavelength of 0.5 μm.

simulations can be performed and instrument performance can be predicted. The difficulty is that the atmospheric turbulence profiles follow a non-stationary process and therefore individual profiles are not representative for use in AO simulations. Of particular interest are the characteristics of the ground-layer and free-atmospheric turbulence, such as the contribution to the total turbulence integral (seeing), thickness and intensity of the ground layer, and if any persistent prominent layers exist.

To characterise the atmospheric turbulence, Model-OTPs have been synthesised from measurements obtained at other

astronomical observatories. Tokovinin & Travouillon (2006) note that previous model-OTPs that are based on the average or median profiles, such as in Abahamid et al. (2004), do not model the strong variability property of turbulence. Abahamid et al. (2004) point out that the turbulence intensity at any given altitude changes by several orders of magnitude and that real OTPs are typically dominated by a few strong layers. Hence, the use of only median or average techniques for OTPs to characterise the atmospheric turbulence for AO analysis may be misleading.

An example is the characterisation of the OTP above the Cerro Pachon (CP) astronomical site. The CP site was

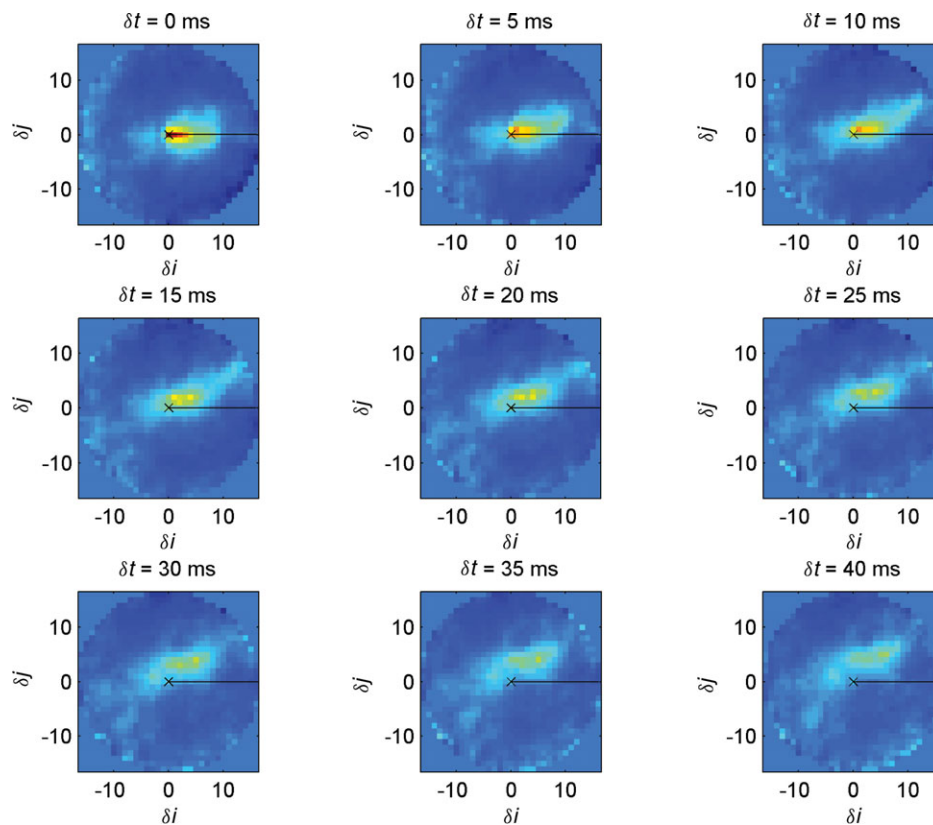**Figure 10.** SSO run 7. Example temporal spatial cross-covariance of centroid data for layer wind speed determination as measured during 2006 April 11–17 with the CCD camera (TM6740GE) having a frame rate of 200 fps (area of interest read-out). The example is of the double star αCen with height resolution $\delta h = 1.0$ km. The double star separation axis (positive heights) is marked with a black line. The temporal offset, τ, is a multiple of the inverse of the frame rate, or 5 ms, starting from the top left panel with $\tau = 0$ ms and the largest offset located at the bottom right panel with $\tau = 40$ ms. The pixels represent the sub-aperture offsets (δi, δj) with physical size $w = 5.8$ cm. The wind speed of a layer can be estimated by s/τ, where s is the physical displacement of the covariance peak for a given temporal offset, τ. For this example, four separate layers are detected with speeds (1) 0.5 m/20 ms = 25 m s^{-1} (8 km); (2) 0.4 m/40 ms = 10 m s^{-1} (4 km); (3) 0.26 m/40 ms = 6.5 m s^{-1} (2 km); and (4) 0.18 m/40 ms = 4.5 m s^{-1} (0 km). Note, $h = 0$ km defines the height of the telescope's primary mirror.

initially characterised during the 1998 Gemini site campaign (Vernin et al. 1998), in which seven discrete layers were modelled by Ellerbroek & Rigaut (2000), referred to as the ER2000 model. The ER2000 model has been used by other groups in AO simulations but is insufficient in two respects as noted by Tokovinin & Travouillon (2006): (i) it does not address the variability of the real OTP and (ii) it was developed for the needs of classical and multi-conjugate AO that is mostly affected by high-altitude turbulence.

To resolve the limitations with the ER2000 model, and other similar models, Tokovinin & Travouillon (2006) propose a new method to derive a more detailed statistical model-OTP suitable for GLAO analysis as well as other AO techniques. The proposed method has already been used by Andersen et al. (2006) to model the OTP for Cerro Pachon for wide-field GLAO simulation for Gemini-South. An outline of the methodology for the model-OTP is given by Tokovinin & Travouillon (2006). Note that the model-OTP

derived in this paper also assumes a Kolmogorov turbulence model.

6.1 Methodology: Layer Strength Model

The model-OTP proposed by Tokovinin & Travouillon (2006) separates the ground-layer (GL) statistics from the free-atmosphere (FA) statistics (observed to be independent). The GL zone is defined from the telescope (10–50 m) to some 500 m above the site. The FA zone is defined as all turbulence above the GL zone.

The Tokovinin & Travouillon (2006) method is well suited to the SLODAR method. The SLODAR method has the ability to measure the GL and FA with sufficient height resolution by choosing appropriate double star separations. The GL can be measured with sufficient height resolution by selecting double stars having the widest separation.

The OTP is universally defined as the dependence of the refractive index structure constant C_N^2 (measured in units $m^{-2/3}$)

at altitude h (measured in units of metres) above sea level (in this paper, $h = 0$ km is the height of the telescope's primary mirror). The turbulence integral, J, is defined as

$$J = \int C_N^2 (h) \mathrm{d}h \qquad (7)$$

(measured in units $m^{1/3}$) and is calculated over some altitude range.

The turbulence integral calculated over the entire height range covering the atmospheric turbulence (0–20 km), the total turbulence strength, can be expressed as the astronomical 'seeing' (in arcsec). The 'seeing' is the spot image FWHM of an unresolved object (e.g., unresolved star). The seeing for observations at a wavelength of $\lambda = 500$ nm at the zenith (Kolmogorov turbulence model) is given by

$$\epsilon = [J/(6.8 \times 10^{-13})]^{0.6}. \qquad (8)$$

As noted by Tokovinin & Travouillon (2006), the seeing is not additive; hence, the preference to use the turbulence integrals, J, which are additive and direct comparisons is possible. The Tokovinin & Travouillon (2006) method calculates the C_N^2 turbulence integral, J, derived from observations for the ground layer (J_{GL}) and the free atmosphere (J_{FA}), then categorises into 'good', 'typical', and 'bad' conditions. The representative 'good' profile is based on an averaged profile representative of the first quartile (25%) of J_{GL} and J_{FA}, based on averaging observational profiles in the range (15%–35%) to ensure an adequate sample size. Likewise, the same goes for the 'typical' profile based on the range (40%–60%) and the 'bad' profile (65%–85%). This process results in a set of three representative profiles for each of the GL and FA that have been averaged separately for each group to reveal typical features.

The Tokovinin & Travouillon (2006) method fits exponential equations to model the GL intensity and thickness. In this paper, we adopt a slightly different approach in that prominent layers are modelled as thin discrete layers, as representative of high-resolution turbulence profiles with micro-thermal balloon measurements. The thin layers preserve the relative strengths as well as the turbulence integrals J_{GL} for the GL and J_{FA} for the FA based on the 'good' (25%), 'typical' (50%), and 'bad' (75%) quartiles.

The J_{GL} was calculated using the 'seeing' parameter (converted to J using Equation 8) and the h_{500} parameter (fractional turbulence below 500 m), using the fact that $J_{\mathrm{GL}} = h_{500}J$. The h_{500} parameter can be calculated for all turbulence profiles as the maximum height is greater than 500 m and the height resolution of the zero height bin is less than 500 m for almost all observations. Hence, the h_{500} parameter is suitable for the calculation of J_{GL}. The J_{FA} was calculated using the fact that $J_{\mathrm{FA}} = J - J_{\mathrm{GL}}$. For the simplicity of calculations, it was assumed that the GL and FA are both modelled by a Kolmogorov turbulence model. With three turbulence profiles based on thin layers for each of the GL and FA, it is possible to construct an OTP model having nine possible outcomes with respective probabilities.

Table 3. Levels of the Cumulative Distributions of J_{GL} Used in the Calculation of a Representative Ground-Layer Profile, 'Good', 'Typical', and 'Bad' for SSO (Runs 1–8: 2005 May to 2006 June)

	Lower	Upper	N_{OTP}	$\overline{H_{\mathrm{max}}}$	$\overline{\delta h}$	$\overline{J_{\mathrm{GL}}}$	$\overline{\epsilon_{\mathrm{GL}}}$
Good	15%	35%	17	1.0728	0.0815	5.1866	0.8483
Typical	40%	60%	10	0.7211	0.1083	8.7999	1.1662
Bad	65%	85%	32	0.7985	0.0722	13.5809	1.5124

The models sufficiently cover half of the conditions (25%–75%) expected at the astronomical site within which a probability of 25% is assigned to 'good', 50% is assigned to 'typical', and 25% is assigned to 'bad' for GL and FA turbulence profiles. The total turbulence profile is a combination of the GL and FA turbulence profiles with probability equal to the respective GL and FA probabilities being multiplied. The assignment of probabilities to all possible turbulence profile outcomes of the model allows a relative importance to be assigned. The model does not sufficiently represent the extreme cases of very 'good' (0%–25%) and very 'bad' (75%–100%) conditions. It is noted that the very 'bad' condition is of most concern as AO may not provide sufficient wavefront correction for scientific operations. Sufficient representation for the very 'good' and very 'bad' conditions can be obtained by extrapolation, scaling the layer relative fractional amounts by the J_{GL} and J_{FA} turbulence integrals, using values from the respective cumulative density function (CDF) plots.

6.1.1 Ground-Layer Model-OTP

To derive the GL model-OTP, we consider three model turbulence profiles derived from averaging a group of observational profiles in intervals centred on the CDF quartiles for the J_{GL} turbulence integral. The 'good' model turbulence profile is derived from averaging profiles having maximum sampling height, H_{max}, greater than 500 m but less than 2 000 m (ground-layer sampling) within the 15%–35% interval of the cumulative values of J_{GL}. Likewise, the same holds for the 'typical' model turbulence profile, within the 40%–60% interval, and the 'bad' model turbulence profile, within the 65%–85% interval. The relatively small value of N_{OTP} for the GL analysis reflects the fact that only a limited number of data sets suitable for GL sampling at SSO were observed. The values relating to the GL model turbulence profiles are listed in Table 3.

From Table 3 we see that some intervals have more turbulence profiles, due to the J_{GL} distribution consisting of a mixture of both GL and FA turbulence profiles, with a portion not meeting the maximum sampling height criterion. The average maximum height range, $\overline{H_{\mathrm{max}}}$, is 0.72–1.07 km and the average height resolution, $\overline{\delta h}$, is 72–108 m.

Figure 11 shows the GL model turbulence profiles obtained from averaging GL profiles within certain interval ranges of the J_{GL} distribution to represent 'good', 'typical', and 'bad' seeing conditions, as summarised in Table 3.
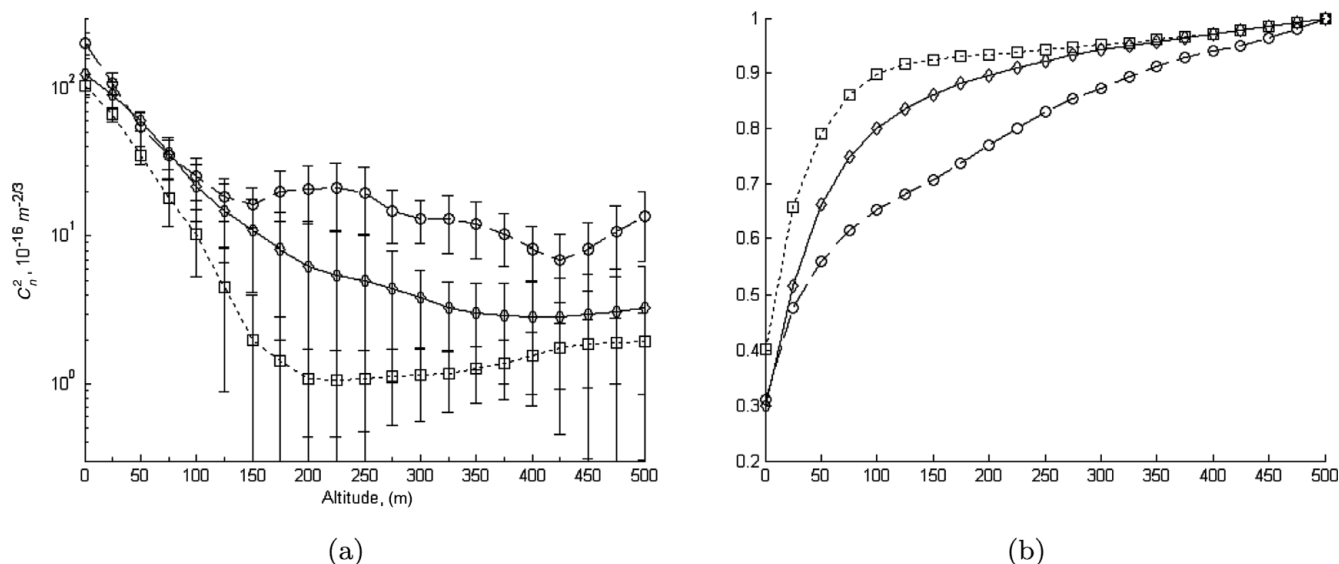
(a)

(b)

Figure 11. Continuous GL model-OTP for SSO (Runs 1–8: 2005 May to 2006 June): squares 'good', diamonds 'typical', and circles 'bad' (a) averaged profiles, error bars are the 95% confidence interval, and (b) corresponding CDF profiles.

Table 4. Turbulence Integrals for the Thin-Layer Model-OTP for the Ground Layer, J in Units of $10^{-13} m^{1/3}$ for SSO (Runs 1–8: 2005 May to 2006 June)

	Range (m)		Integral, J		
Layer Height (m)	Lower	Upper	Good	Typical	Bad
37.5	0	150	4.6104	6.9491	8.3327
250	150	350	0.2431	1.0870	3.3985
Total (37.5 + 250)			4.8535	8.0361	11.7312
Integral (0–500)	0	500	5.1866	8.7999	13.5809
% Explained			93.5782	91.3203	86.3805

Table 5. Final Turbulence Integrals for the GL Thin-Layer Model-OTP, J in Units of $10^{-13} m^{1/3}$ for SSO (Runs 1–8: 2005 May to 2006 June)

	Model Integral, J		
Layer Height (m)	Good	Typical	Bad
37.5	4.7129	7.3989	9.4363
250	0.2485	1.1574	3.8486
Total (37.5 + 250)	4.9614	8.5562	13.2849
ϵ_{GL}	0.8277	1.1478	1.4945
Probability	25%	50%	25%

A thin-layer GL model-OTP is required to be derived from the continuous GL model-OTP. A thin-layer GL model-OTP is an accurate representation of high-resolution OTPs (Azouit & Vernin 2005), as well as compatible for AO simulations (using phase screens to represent thin layers). For the thin-layer GL model-OTP, we define two layers at heights 37.5 and 250 m to best represent the continuous GL model-OTP (Figure 11). To calculate the strengths of the layers, an integral (lower, upper) centred on the layer heights of the continuous GL model-OTP is performed. To compare how well layer integrals explain the model, the total layer integral (37.5 m + 250 m) is compared with the total GL integral from 0 to 500 m (calculated from the continuous GL model-OTP). The results are listed in Table 4.

The fractional strengths can be multiplied by J_{GL} according to cumulative level values obtained from its corresponding CDF plot. The model is based on the cumulative levels 25%, 50%, and 75%, but other levels can be used for ex-

treme conditions, e.g. 10%, 50%, and 90%, providing some flexibility for a custom model-OTP.

The turbulence integral strengths of the model thin layers are calculated by multiplying the fractional amounts with the cumulative levels 25%, 50%, and 75% of J_{GL}. The final model thin layers and their turbulence integral, with total ground-layer seeing, ϵ_{GL}, and model probability, are listed in Table 5.

6.1.2 Free-Atmosphere Model-OTP

To derive the FA model, we follow a similar approach to that described for the GL model. This involves deriving three model turbulence profiles from averaging a group of observational profiles within representative intervals of CDF values for the J_{FA} turbulence integral. The 'good' model turbulence profile is derived from averaging profiles having maximum sampling height, H_{max}, greater than 16 000 m but less than 20 000 m (free-atmosphere sampling) within the 15%–35% interval of the cumulative values of J_{FA}. Likewise, the same

Table 6. Levels of the Cumulative Distributions of J_{FA} Used in the Calculation of a Representative Ground-Layer Profile, 'Good', 'Typical', and 'Bad' for SSO (Runs 1–8: 2005 May to 2006 June)

	Lower	Upper	N_{OTP}	$\overline{H_{max}}$	$\overline{\delta h}$	$\overline{J_{GL}}$	$\overline{\epsilon_{GL}}$
Good	15%	35%	147	17.0076	1.0951	0.3702	0.1719
Typical	40%	60%	118	17.1918	1.3382	1.1983	0.3509
Bad	65%	85%	58	17.3392	1.1926	2.5276	0.5503

holds for the 'typical' model turbulence profile, within the 40%–60% interval, and the 'bad' model turbulence profile, within the 65%–85% interval. The values relating to the FA model turbulence profiles are listed in Table 6.

From Table 6 we see that some intervals have more turbulence profiles, due to the J_{FA} distribution consisting of a mixture of both GL and FA turbulence profiles, with a portion not meeting the maximum sampling height criteria. The average maximum height range, $\overline{H_{max}}$, is 17.0–17.3 km and the average height resolution, $\overline{\delta h}$, is 1 095–1 338 m.

Figure 12 shows the FA model turbulence profiles obtained from averaging FA profiles within certain interval ranges of the J_{FA} distribution to represent 'good', 'typical', and 'bad' seeing conditions, as summarised in Table 6.

A thin-layer FA model-OTP is required to be derived from the continuous FA model-OTP. A thin-layer FA model-OTP is an accurate representation of high-resolution OTPs (Azouit & Vernin 2005) as well as compatible for adaptive optic simulations (using phase screens to represent thin layers). For the thin-layer FA model-OTP, we define five layers at heights 1 000, 3 000, 6 000, 9 000, and 13 500 m to best represent the continuous FA model-OTP (Figure 12). To calculate the strengths of the layers, an integral (lower, upper) centred on the layer heights of the continuous FA model-OTP is performed. To compare how well layer integrals explain the model, the total layer integral (1 000 + 3 000 + 6 000 + 9 000 + 13 500 m) is compared with the total FA integral from 500 to 16 000 m (calculated from the continuous FA model-OTP). The results are listed in Table 7.

The FA model-OTP in Table 7 has a gap in binning between 10.5 and 12 km as well above 15 km. This is because we rarely saw any evidence for turbulence at those heights in the continuous FA profile of Figure 12. There was also an attempt to keep the number of model layers to minimum as well as keeping equal bin widths of 3000 m. The gap in binning will result in a slight bias to increase the relative strength of the FA lower layers, causing the isoplanatic angle to be slightly larger (providing an optimistic estimate). The value of the bias is expected to be small.

The fractional strengths can be multiplied by J_{FA} according to cumulative levels obtained from its CDF plot. The model is based on the cumulative levels 25%, 50%, and 75%, but for other levels extreme conditions can be used, e.g. 10%, 50%, and 90%, providing some flexibility for a custom model-OTP.

The turbulence integral strengths of the model thin layers are calculated by multiplying the fractional amounts with

Table 7. Turbulence Integrals for the Thin-Layer Model-OTP for the Free Atmosphere, J in Units of $10^{-13}m^{1/3}$ for SSO (Runs 1–8: 2005 May to 2006 June)

	Range (m)		Integral, J		
Layer Height (m)	Lower	Upper	Good	Typical	Bad
1 000	500	1 500	0.0770	0.2577	0.3675
3 000	1 500	4 500	0.0100	0.2358	0.6265
6 000	4 500	7 500	0.0065	0.0499	0.1974
9 000	7 500	10 500	0.0093	0.0466	0.1222
13 500	12 000	15 000	0.0209	0.0641	0.1810
Total (1 000 + 3 000 + 6 000 + 9 000 + 13 500)			0.1237	0.6541	1.4946
Integral (500–16 000)	500	16 000	0.1409	0.7032	1.6387
% Explained			87.7795	93.0185	91.2053

Table 8. Final Turbulence Integrals for the FA Thin-Layer Model-OTP, J in Units of $10^{-13}m^{1/3}$ for SSO (Runs 1–8: 2005 May to 2006 June)

	Model Integral, J		
Layer Height (m)	Good	Typical	Bad
1 000	0.2413	0.4772	0.6677
3 000	0.0315	0.4368	1.1384
6 000	0.0204	0.0924	0.3588
9 000	0.0291	0.0863	0.2221
13 500	0.0656	0.1187	0.3289
Total (3 000 + 6 000 + 9 000 + 13 500)	0.3880	1.2115	2.7159
ϵ_{FA}	0.1794	0.3552	0.5766
Probability	25%	50%	25%

the cumulative levels 25%, 50%, and 75% of J_{FA}. The final model thin layers and their turbulence integral, with the total free-atmosphere seeing, ϵ_{FA}, and model probability, are listed in Table 8.

The total integrated turbulence of the thin-layer FA model as shown in Table 8 is approximately twice that of the total integrated turbulence of the binned layer continuous FA model as shown in Table 7. A likely explanation for the scale factor of ∼2 may be the result that the parameter J_{FA} has been overestimated (turbulence integral in the free atmosphere computed based on total seeing and H_{500}) compared with the direct turbulence integrals of the averaged measured profiles. The total strength of the weaker free-atmosphere layers (not location) as measured by SLODAR is somewhat underestimated (low S/N). The factor of a ∼2 scaling increase makes the free-atmosphere seeing in the final model a conservative estimate.
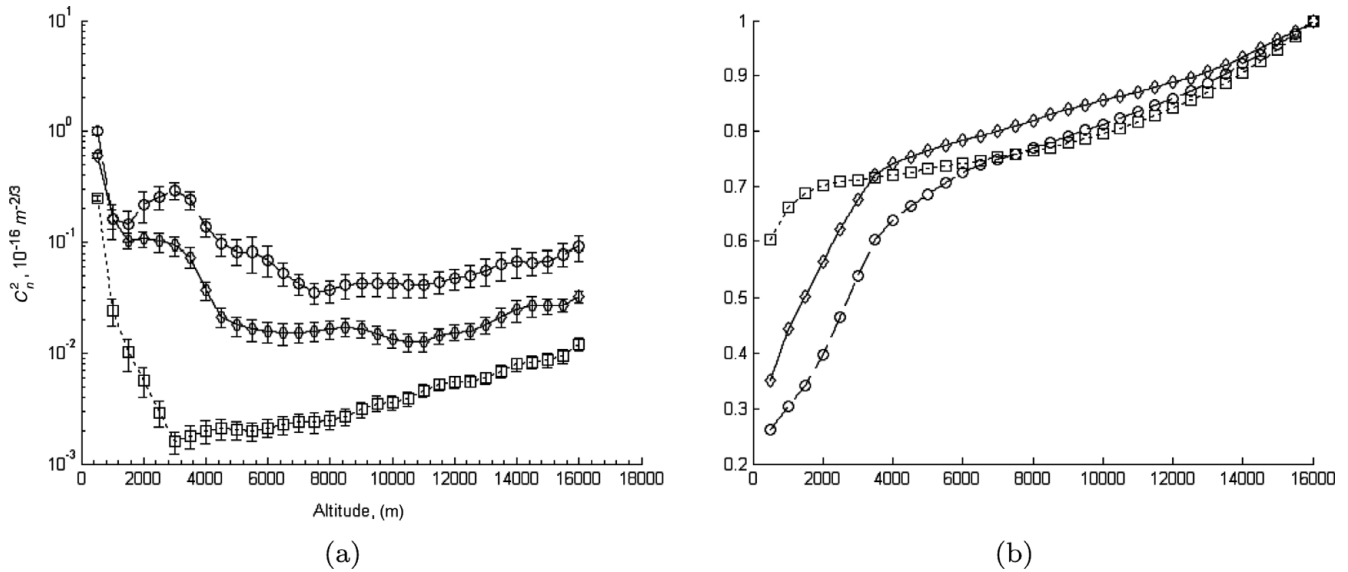
Figure 12. Continuous FA model-OTP for SSO (Runs 1–8: 2005 May to 2006 June): squares 'good', diamonds 'typical', and circles 'bad' (a) averaged profiles, error bars are the 95% confidence interval, and (b) corresponding CDF profiles.

Table 9. Bufton Wind Model

	v_G	v_T	H_T	L_T
Good	2	30	9 000	4 000
Typical	5	35	10 000	5 000
Bad	8	40	11 000	6 000

6.2 Methodology: Layer Wind Speed and Direction Model

To model the turbulent layer speeds, a Bufton wind speed profile model is used (see Equation 9). To model the 'good', 'typical', and 'bad' conditions, three separate Bufton wind profiles are presented based on data found in the literature (Avila et al. 2003; Tokovinin, Baumont, & Vasquez 2003; Azouit & Vernin 2005). The wind profiles are not based on fits to our data as it is not always possible to obtain a sufficient sample of layer wind speeds with our SLODAR data due to (i) low camera frame rates, (ii) finite camera exposures, (iii) weakness of a layer, and (iv) short boiling lifetimes (layer de-correlates rapidly). The Bufton wind profile model is given by

$$v(h) = v_G + v_T \exp\left[-\left(\frac{h - H_T}{L_T} \right)^2 \right], \quad (9)$$

where v_G denotes the wind velocity at low altitude, v_T denotes the wind velocity at the tropopause, H_T denotes the height of tropopause, L_T denotes the thickness of the tropopause layer.

The parameters of the Bufton wind model for the 'good', 'typical', and 'bad' conditions used in the analysis are listed in Table 9. The wind model associates strong ground-layer wind speeds with stronger free-atmosphere wind speeds that

have a broader upper atmosphere extent (Azouit & Vernin 2005; Tokovinin et al. 2003; Avila et al. 2003). To simplify the model, the 'good', 'typical', and 'bad' conditions are represented by the same profile and referenced to the ground-layer wind direction, set to 0°. The free-atmosphere layers can travel in a direction perpendicular to the ground-layer direction. The wind direction model, $\psi(h)$, for the 'good', 'typical', and 'bad' conditions is defined as

$$\psi(h) = a(1 - \exp(-h/b)) \quad (10)$$

where $a = 101.93$ and $b = 3\,255.4$ are used.

6.2.1 Turbulent-Layer Wind Model

To model the turbulent-layer wind speed and direction for the SSO (runs 1–8: 2005 May to 2006 June) runs, a Bufton wind speed model together with layer height information from the model-OTP is used. The model-OTP layer heights for the ground layer and free atmosphere are used in the Bufton equation to obtain the model layer wind speed values. The model relative layer wind directions are obtained by using the model-OTP layer heights in the wind direction, $\phi(h)$, defined in Equation (10). The wind speed model and wind direction model values for the SSO (runs 1–8: 2005 May to 2006 June) model-OTP are shown in Figure 13 and tabulated in Table 10.

6.3 Summary Model-OTP

The summary model-OTP (Kolmogorov) is the combination of the 'good', 'typical', and 'bad' GL and FA model-OTPs resulting in a set of nine possible thin-layer turbulence profiles. Each turbulence profile of the model-OTP includes informa-
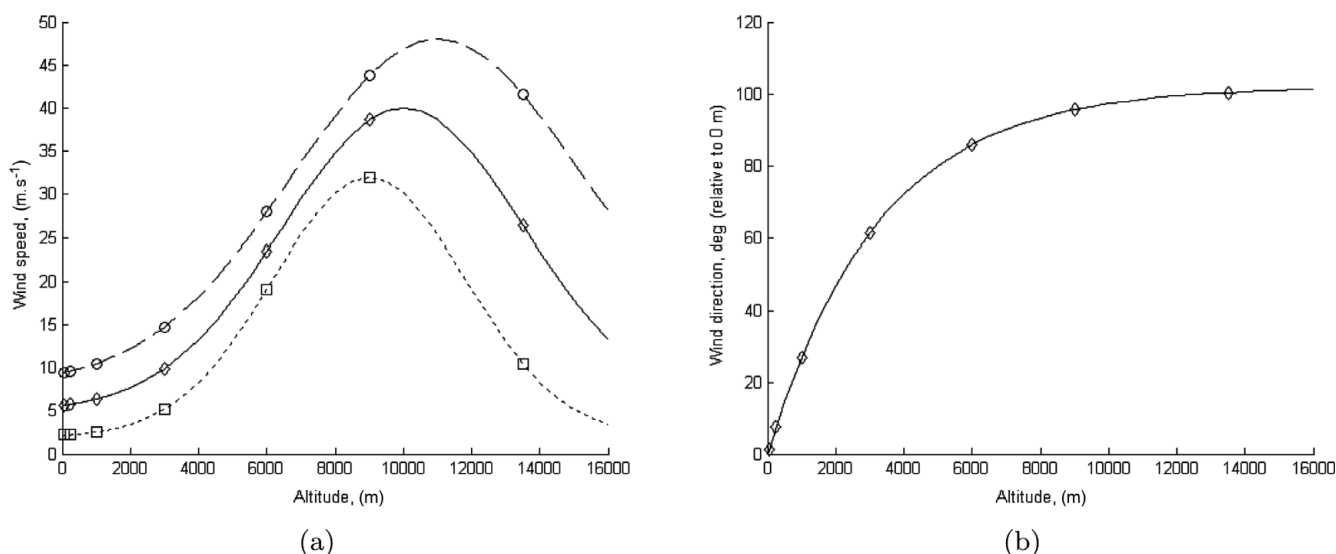
(a)

(b)

Figure 13. Wind model-OTP for the SSO (Runs 1–8: 2005 May to 2006 June) runs: squares 'good', diamonds 'typical', and circles 'bad' (a) Bufton wind profile and (b) wind direction (empirical). Layer heights for model-OTP for the SSO (Runs 1–8: 2005 May to 2006 June) model are marked as symbols.

Table 10. Tabulated Values for the Model Wind Speed and Model Wind Direction for the GL and FA Model-OTP Layers for the SSO (Runs 1–8: 2005 May to 2006 June) Model

	Height (m)	Bufton Wind Speed Model (m s^{-1})			Wind Direction (deg, ref 0 m)
		Good	Typical	Bad	
GL	37.5	2.1981	5.6605	9.4200	1.1674
	250	2.2506	5.7810	9.6142	7.5347
FA	1 000	2.5495	6.3707	10.4871	26.9588
	3 000	5.1620	9.9300	14.7605	61.3717
	6 000	19.0935	23.4552	27.9741	85.7917
	9 000	32.0000	38.6276	43.7936	95.5085
	13 500	10.4619	26.4419	41.6249	100.3182

tion about the turbulence layer strength, wind speed, and wind direction.

A detailed summary table of the summary model-OTPs describing the observations at Siding Spring Observatory, Australia, for the SSO (runs 1–8: 2005 May to 2006 June) runs is presented in Table 11 (turbulence integrals), Table 12 (turbulence layer wind speeds), and Table 13 (turbulence layer wind direction). Note that the model-OTP seeing, ϵ, for the typical GL + FA of 1.24 arcsec is similar to the historical median DIMM seeing of 1.25 arcsec reported by Wood et al. (1995).

7 CONCLUSIONS

This paper has reported on our turbulence profiling observational results performed at SSO. A summary of results with example data has been presented for measurement spanning years 2005 to 2006 using the 7 × 7 (runs 1–6) and 17 × 17 (runs 7 and 8) SLODAR instruments. The observational

results have facilitated the site characterisation of the optical turbulence profile with the implementation of the model-OTP (Kolmogorov) for SSO. The model-OTP describes the turbulence layer strength (Table 11), layer wind speed (Table 12), and layer wind direction (Table 13). The model-OTP is useful for the prediction of AO performance at SSO (forthcoming paper) using simulation codes. Prior to the commencement of our SLODAR campaign, the seeing statistics were relatively well understood with DIMM seeing measurements (Wood et al. 1995), whereas the vertical structure of the turbulence profile structure was relatively unknown, with only a few SCIDAR profiles reported by Klueckers et al. (1998). The following conclusions can be stated about the atmospheric turbulence above SSO based on our data:

- A measured median atmospheric seeing of around 1.2 arcsec (Kolmogorov model with mirror/dome seeing removed). The seeing is discussed in Section 5.1.

Table 11. Tabulated Values for the Final Model-OTP for SSO (Runs 1–8: 2005 May to 2006 June), with Layers Specified as Turbulence Integral, J, in Units $10^{-13}m^{1/3}$

| | | Model Turbulence Profiles (J, Integral) – SSO (Runs 1–8: 2005 May to 2006 June) | | | | | | | | |
| | GL | Good | | | Typical | | | Bad | | |
Parameter	FA Units	Good 1	Typical 2	Bad 3	Good 4	Typical 5	Bad 6	Good 7	Typical 8	Bad 9
37.5	$10^{-13}m^{1/3}$	4.7129	4.7129	4.7129	7.3989	7.3989	7.3989	9.4363	9.4363	9.4363
250	$10^{-13}m^{1/3}$	0.2485	0.2485	0.2485	1.1574	1.1574	1.1574	3.8486	3.8486	3.8486
1 000	$10^{-13}m^{1/3}$	0.2413	0.4772	0.6677	0.2413	0.4772	0.6677	0.2413	0.4772	0.6677
3 000	$10^{-13}m^{1/3}$	0.0315	0.4368	1.1384	0.0315	0.4368	1.1384	0.0315	0.4368	1.1384
6 000	$10^{-13}m^{1/3}$	0.0204	0.0924	0.3588	0.0204	0.0924	0.3588	0.0204	0.0924	0.3588
9 000	$10^{-13}m^{1/3}$	0.0291	0.0863	0.2221	0.0291	0.0863	0.2221	0.0291	0.0863	0.2221
13 500	$10^{-13}m^{1/3}$	0.0656	0.1187	0.3289	0.0656	0.1187	0.3289	0.0656	0.1187	0.3289
J_{GL}	$10^{-13}m^{1/3}$	4.9614	4.9614	4.9614	8.5562	8.5562	8.5562	13.2849	13.2849	13.2849
J_{FA}	$10^{-13}m^{1/3}$	0.3880	1.2115	2.7159	0.3880	1.2115	2.7159	0.3880	1.2115	2.7159
J	$10^{-13}m^{1/3}$	5.3493	6.1729	7.6773	8.9442	9.7678	11.2721	13.6728	14.4964	16.0008
F_{GL}	/1.0	0.9275	0.8037	0.6462	0.9566	0.8760	0.7591	0.9716	0.9164	0.8303
F_{FA}	/1.0	0.0725	0.1963	0.3538	0.0434	0.1240	0.2409	0.0284	0.0836	0.1697
ϵ_{GL}	arcsec	0.8277	0.8277	0.8277	1.1478	1.1478	1.1478	1.4945	1.4945	1.4945
ϵ_{FA}	arcsec	0.1794	0.3552	0.5766	0.1794	0.3552	0.5766	0.1794	0.3552	0.5766
ϵ	arcsec	0.8659	0.9436	1.0755	1.1787	1.2427	1.3542	1.5206	1.5749	1.6710
θ_0	arcsec	6.4233	3.7172	2.0123	6.3684	3.7043	2.0098	6.2255	3.6700	2.0030
τ	ms	11.7922	5.3516	2.3291	4.5855	3.5038	2.0310	2.2067	2.0112	1.5242
Probability	/1.0	0.0625	0.1250	0.0625	0.1250	0.2500	0.1250	0.0625	0.1250	0.0625

Table 12. Tabulated Values for the Final Model-OTP for the SSO (Runs 1–8: 2005 May to 2006 June), with Layers Specified as Wind Speeds

| | | Model Turbulence Profiles (Layer Wind Speeds) – SSO (Runs 1–8: 2005 May to 2006 June) | | | | | | | | |
| | GL | Good | | | Typical | | | Bad | | |
Parameter	FA Units	Good 1	Typical 2	Bad 3	Good 4	Typical 5	Bad 6	Good 7	Typical 8	Bad 9
37.5	m s^{-1}	2.1981	2.1981	2.1981	5.6605	5.6605	5.6605	9.4200	9.4200	9.4200
250	m s^{-1}	2.2506	2.2506	2.2506	5.7810	5.7810	5.7810	9.6142	9.6142	9.6142
1 000	m s^{-1}	2.5495	6.3707	10.4871	2.5495	6.3707	10.4871	2.5495	6.3707	10.4871
3 000	m s^{-1}	5.1620	9.9300	14.7605	5.1620	9.9300	14.7605	5.1620	9.9300	14.7605
6 000	m s^{-1}	19.0935	23.4552	27.9741	19.0935	23.4552	27.9741	19.0935	23.4552	27.9741
9 000	m s^{-1}	32.0000	38.6276	43.7936	32.0000	38.6276	43.7936	32.0000	38.6276	43.7936
13 500	m s^{-1}	10.4619	26.4419	41.6250	10.4619	26.4419	41.6250	10.4619	26.4419	41.6250
J_{GL}	$10^{-13}m^{1/3}$	4.9614	4.9614	4.9614	8.5562	8.5562	8.5562	13.2849	13.2849	13.2849
J_{FA}	$10^{-13}m^{1/3}$	0.3880	1.2115	2.7159	0.3880	1.2115	2.7159	0.3880	1.2115	2.7159
J	$10^{-13}m^{1/3}$	5.3493	6.1729	7.6773	8.9442	9.7678	11.2721	13.6728	14.4964	16.0008
F_{GL}	/1.0	0.9275	0.8037	0.6462	0.9566	0.8760	0.7591	0.9716	0.9164	0.8303
F_{FA}	/1.0	0.0725	0.1963	0.3538	0.0434	0.1240	0.2409	0.0284	0.0836	0.1697
ϵ_{GL}	arcsec	0.8277	0.8277	0.8277	1.1478	1.1478	1.1478	1.4945	1.4945	1.4945
ϵ_{FA}	arcsec	0.1794	0.3552	0.5766	0.1794	0.3552	0.5766	0.1794	0.3552	0.5766
ϵ	arcsec	0.8659	0.9436	1.0755	1.1787	1.2427	1.3542	1.5206	1.5749	1.6710
θ_0	arcsec	6.4233	3.7172	2.0123	6.3684	3.7043	2.0098	6.2255	3.6700	2.0030
τ	ms	11.7922	5.3516	2.3291	4.5855	3.5038	2.0310	2.2067	2.0112	1.5242
Probability	/1.0	0.0625	0.1250	0.0625	0.1250	0.2500	0.1250	0.0625	0.1250	0.0625

Table 13. Tabulated Values for the Final Model-OTP for the SSO (Runs 1–8: 2005 May to 2006 June), with Layers Specified as Wind Directions

Parameter	GL / FA Units	Good			Typical			Bad		
		Good 1	Typical 2	Bad 3	Good 4	Typical 5	Bad 6	Good 7	Typical 8	Bad 9
37.5	deg	1.1674	1.1674	1.1674	1.1674	1.1674	1.1674	1.1674	1.1674	1.1674
250	deg	7.5347	7.5347	7.5347	7.5347	7.5347	7.5347	7.5347	7.5347	7.5347
1 000	deg	26.9588	26.9588	26.9588	26.9588	26.9588	26.9588	26.9588	26.9588	26.9588
3 000	deg	61.3717	61.3717	61.3717	61.3717	61.3717	61.3717	61.3717	61.3717	61.3717
6 000	deg	85.7917	85.7917	85.7917	85.7917	85.7917	85.7917	85.7917	85.7917	85.7917
9 000	deg	95.5085	95.5085	95.5085	95.5085	95.5085	95.5085	95.5085	95.5085	95.5085
13 500	deg	100.3182	100.3182	100.3182	100.3182	100.3182	100.3182	100.3182	100.3182	100.3182
J_{GL}	$10^{-13} m^{1/3}$	4.9614	4.9614	4.9614	8.5562	8.5562	8.5562	13.2849	13.2849	13.2849
J_{FA}	$10^{-13} m^{1/3}$	0.3880	1.2115	2.7159	0.3880	1.2115	2.7159	0.3880	1.2115	2.7159
J	$10^{-13} m^{1/3}$	5.3493	6.1729	7.6773	8.9442	9.7678	11.2721	13.6728	14.4964	16.0008
F_{GL}	/1.0	0.9275	0.8037	0.6462	0.9566	0.8760	0.7591	0.9716	0.9164	0.8303
F_{FA}	/1.0	0.0725	0.1963	0.3538	0.0434	0.1240	0.2409	0.0284	0.0836	0.1697
ϵ_{GL}	arcsec	0.8277	0.8277	0.8277	1.1478	1.1478	1.1478	1.4945	1.4945	1.4945
ϵ_{FA}	arcsec	0.1794	0.3552	0.5766	0.1794	0.3552	0.5766	0.1794	0.3552	0.5766
ϵ	arcsec	0.8659	0.9436	1.0755	1.1787	1.2427	1.3542	1.5206	1.5749	1.6710
θ_0	arcsec	6.4233	3.7172	2.0123	6.3684	3.7043	2.0098	6.2255	3.6700	2.0030
τ	ms	11.7922	5.3516	2.3291	4.5855	3.5038	2.0310	2.2067	2.0112	1.5242
Probability	/1.0	0.0625	0.1250	0.0625	0.1250	0.2500	0.1250	0.0625	0.1250	0.0625

- Ground-layer turbulence dominates, with ∼80% turbulence below 500 m (h_{500}). The structure of the turbulence is discussed in Section 5.1. The presence of a strong ground layer was also discovered during site measurements at Mount John University Observatory (Mohr, Johnston, & Cottrell 2010). The dominant ground layer has promising implications for GLAO. A forthcoming paper will investigate the performance of GLAO based on the model-OTP for SSO.
- Non-Kolmogorov turbulence is observed especially for ground layer, with $\beta_{avg} \sim 10/3$. The power-law slope of the spatial phase fluctuations is discussed in Section 5.1. The non-Kolmogorov spectrum results in a different scaling of seeing with wavelength to that conventionally assumed.
- Turbulence profiles show a number of dynamical characteristics: (i) are most intense near the ground (below 100 m) and (ii) fluctuate in intensity, appearing in 'bursts' with timescales of several minutes. These characteristics are shown in Figure 6 as a sequence of turbulence profiles.
- Mirror/dome seeing can be a significant fraction of the ground-layer turbulence. This is evident as a zero-height static contribution in the turbulent-layer wind speed measurements (refer to Section 5.2 and Figure 10).
- The free-atmosphere turbulence is comparable to 'good' seeing sites. From the model-OTP shown in Table 11, the free-atmosphere seeing for SSO is 0.18 (25%), 0.36 (50%), and 0.58 (75%) arcsec. The Cerro Pachon (see-

ing ∼0.75) model (Tokovinin & Travouillon 2006) for the free-atmosphere reports 0.29 (25%), 0.40 (50%), and 0.55 (75%) arcsec.

REFERENCES

Abahamid, A., Jabiri, A., Vernin, J., Benkhaldoun, Z., Azouit, M., & Agabi, A. 2004, A&A, 416, 1193
Andersen, D. R., et al. 2006, PASP, 118, 1574
Avila, R., et al. 2003, RMxAC, 27, 11
Azouit, M. & Vernin, J. 2005, PASP, 117, 536
Butterley, T., Wilson, R. W., & Sarazin, M. 2006, MNRAS, 369, 835
Ellerbroek, B. L. & Rigaut, F. J. 2000, Proc. SPIE, 4007, 1088
Fried, D. L. 1966, J. Opt. Soc. Am., 56, 1372
Fried, D. L. 1982, J. Opt. Soc. Am., 72, 52
Fuchs, A., Tallon, M., & Vernin, J. 1994, Proc. SPIE, 2222, 682
Goodwin, M. 2009, ANU PhD thesis

Goodwin, M., Jenkins, C., & Lambert, A. 2007, Opt. Express, 151, 14844

Greenwood, D. P. 1977, J. Opt. Soc. Am., 67, 390

Hardy, J. W. 1998, Adaptive Optics for Astronomical Telescopes (Oxford: Oxford University Press)

Hubin, N., et al. 2006, IAUS, 232, 60

JAI Inc. 2009, Pulnix, http://www.jai.com/

Klueckers, V. A., Wooder, N. J., Nicholls, T. W., Adcock, M. J., Munro, I., & Dainty, J. C. 1998, A&AS, 130, 141

MathWorks 2005, MATLAB v7.0.4.365 (R14) Service Pack 2, http://www.mathworks.com/products/matlab/

Mohr, J. L., Johnston, R. A., & Cottrell, P. L. 2010, PASA, 27, 347

Pant, P., Stalin, C. S., & Sagar, R. 1999, A&AS, 136, 19

PixeLINK 2009, Pixelink, http://www.pixelink.com/

Sarazin, M., Butterley, T., Tokovinin, A., Travouillon, T., & Wilson, R. 2005, The Tololo SLODAR Campaign, Final Report, https://www.eso.org/genfac/pubs/astclim/paranal/asm/slodar/The Tololo SLODAR Campaign.htm

Stribling, B. E., Welsh, B. M., & Roggemann, M. C. 1995, Proc. SPIE, 2471,181

Tokovinin, A., Baumont, S., & Vasquez, J. 2003, MNRAS, 340, 52

Tokovinin, A. & Travouillon, T. 2006, MNRAS, 365, 1235

Travouillon, T. 2006, Proc. SPIE, 6267, 626720

Vernin, J., et al. 1998, 1998 Gemini site testing campaign, Cerro Pachon and Cerro Tololo, Gemini Report RPT-AO-G0094

Vernin, J. & Roddier, F. 1973, J. Opt. Soc. Am., 63, 270

Wilson, R. W. 2002, MNRAS, 337, 103

Wood, P. R., Rodgers, A. W., & Russell, K. S. 1995, PASA, 12, 97